ACS APPLIED MATERIALS & INTERFACES

www.acsami.org

Research Article

CelluPhot: Hybrid Cellulose–Bismuth Oxybromide Membrane for Pollutant Removal

Joy Onwumere, Jędrzej Piątek, Tetyana Budnyak, Jianhong Chen, Serhiy Budnyk, Zoheb Karim, Thomas Thersleff, Piotr Kuśtrowski, Aji P. Mathew,* and Adam Slabon*

Cite This: *ACS Appl. Mater. Interfaces* 2020, 12, 42891–42901

Read Online

ACCESS | Metrics & More | Article Recommendations | Supporting Information

ABSTRACT: The simultaneous removal of organic and inorganic pollutants from wastewater is a complex challenge and requires usually several sequential processes. Here, we demonstrate the fabrication of a hybrid material that can fulfill both tasks: (i) the adsorption of metal ions due to the negative surface charge, and (ii) photocatalytic decomposition of organic compounds. The bioinorganic hybrid membrane consists of cellulose fibers to ensure mechanical stability and of $Bi_4O_5Br_2$/BiOBr nanosheets. The composite is synthesized at low temperature of 115 °C directly on the cellulose membrane (CM) in order to maintain the carboxylic and hydroxyl groups on the surface that are responsible for the adsorption of metal ions. The composite can adsorb both Co(II) and Ni(II) ions and the kinetic study confirmed a good agreement of experimental data with the pseudo-second-order equation kinetic model. CM/$Bi_4O_5Br_2$/BiOBr showed higher affinity to Co(II) ions than to Ni(II) ions from diluted aqueous solutions. The bioinorganic composite demonstrates a synergistic effect in the photocatalytic degradation of rhodamine B (RhB) by exceeding the removal efficiency of single components. The fabrication of the biologic-inorganic interface was confirmed by various analytical techniques including scanning electron microscopy (SEM), scanning transmission electron microscopy with energy dispersive X-ray spectroscopy (STEM EDX) mapping, X-ray diffraction (XRD), and X-ray photoelectron spectroscopy (XPS). The presented approach for controlled formation of the bioinorganic interface between natural material (cellulose) and nanoscopic inorganic materials of tailored morphology (Bi–O–Br system) enables the significant enhancement of materials functionality.

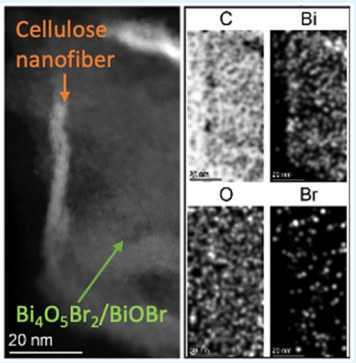

KEYWORDS: *photocatalysis, bioinorganic interface, cellulose composites, semiconductor heterojunctions, adsorption of metal ions*

INTRODUCTION

The removal of both organic and inorganic pollutants from wastewater is one of the critical aspects that have to be considered for human health. Organic dyes and pigments are common water pollutants, which are produced in large scale by textile, dyeing, paper and pulp, cosmetic, food, and paint industries.[1−3] In addition, many dyes are reluctant to biodegrade and could be harmful to human health due to their toxic character. In some cases, they are even carcinogenic.[4,5] An example is rhodamine B (**RhB**), which is a typical fluorescent (xanthene) dye and is highly soluble in water. The carcinogenicity and toxicity, including neurotoxicity toward humans and animals, have been proven experimentally.[6−9] Conventional methods of removal of dyes include precipitation/separation of pollutants, coagulation by a chemical agent, ozone oxidation, or hypochlorite oxidation. For the latter method, the formation of halogenated organic products is still a challenging issue. In comparison to known techniques, photocatalytic decomposition of dyes as pollutant on semiconducting materials is expected to be a prospective alternative.[10]

The remediation of complex metal−ion composition in industrial wastes can be achieved by variety of methods including precipitation, chemisorption, membrane filtration, but this methodology requires aggressive chemicals and is inevitably connected to the production of solid waste, which cannot be valorized into raw materials for further application. Alternatively, metal ions can be recovered at near-neutral pH values on membranes that can adsorb the metal ions by Coulombic attraction, but short life cycle of the membranes, poor functionality in aggressive manufacturing conditions, and problematic recyclability remain limiting criteria for their extensive technical applications. Among promising membrane materials, cellulose has been identified as a sustainable candidate, because it offers several advantages. Cellulose as a biomaterial is one of the most naturally abundant biodegradable polymers.[11,12] It consists of polysaccharides with high amount of glucose and hydroxyl groups.[11,13] Cellulose-based materials are characterized by renewability, biodegradability,

Received: July 15, 2020
Accepted: August 25, 2020
Published: August 25, 2020

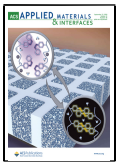

biocompatibility,[12] and insolubility,[14] and can be tailored with respect to mechanical stability, morphology, and controlled growth of nanostructures.[15] Hydroxylic and carboxylic groups of cellulose can effectively bind metal cations by means of chemical, coordination, or physicochemical methods and remove them from liquid media, such as wastewater.

The integration of biobased materials, such as cellulose, lignin, or chitosan, with binary oxides has led to the development of sorbents that are characterized by ameliorated kinetics.[16,17] For instance, bioinorganic composites of lignin are highly efficient as sorbents for removal of metal ions.[18] In the case of cellulose as sorbent material, hybrids have been prepared including metal−organic frameworks (MOFs)[19] and metal oxide particles.[20,21]

Mixed-anion bismuth compounds BiOX (X = Cl, Br, I) and Bi_2O_2NCN belong to the category of two-dimensional layered semiconductor photocatalysts with $[Bi_2O_2]^{2+}$ slabs interleaved by double slabs of the second counteranion X.[22−30] Besides their intriguing crystal chemistry, this class of compounds exhibits potential photocatalytic activity due to their semiconducting properties.[22−24,31] A representative for a p-type semiconductor among this class of compounds is BiOBr.[32] The latter displays a high chemical stability under light irradiation and makes it applicable for different photochemical reactions.[26,30−34] Due to its lamellar structure, BiOBr belongs to group of low-dimensional nanostructures, which are of high interest for photocatalytic applications because of more efficient charge carrier separation in comparison to bulk materials.[35−40] Since BiOBr can harvest more light than bismuth oxychlorides and oxyiodates, originating from the narrower band gap of 2.7−2.9 eV, it exhibits relatively high photocatalytic activity.[31,32,41] Despite the above-mentioned advantage, pristine BiOBr has a limited practical application as photocatalyst due to the high recombination rate of photogenerated electron−hole pairs and the low light absorption efficiency.

A general strategy to improve charge carrier separation is the formation of semiconductor heterostructures. Several different ternary bismuth oxybromides are known from the literature, such as $Bi_{12}O_{17}Br_2$, Bi_5O_7Br, Bi_3O_4Br, $Bi_{24}O_{31}Br_{10}$, and $Bi_4O_5Br_2$.[23,24,42] Su[43] et al. synthesized $Bi_4O_5Br_2$/BiOBr heterojunctions with a plate-like structure by an one-pot hydrothermal method, whereas Panje et al. synthesized $Bi_4O_5Br_2$/BiOBr flower-like nanostructures. Increasing the bismuth content in the Bi−O−Br system is known to result in a negative shift of the conduction band. This results also in a reduction of the band gap and improves consequently the light absorption efficiency.[24,42−44] Several inorganic and bioinorganic composites have been previously successfully demonstrated to be sorbents and sensors for both cobalt and nickel ions, which has motivated us to develop low-cost bioinorganic hybrids with dual functionality.[45−54] Given the recent increased interest in mixed-anion compounds from this ternary system, we were interested in developing a low-temperature synthesis that would allow integration with renewable materials, such as cellulose.

In the present work, we report on the fabrication of a bioinorganic hybrid material that combines photocatalytic properties while being simultaneously a sorbent material. We have chosen cellulose as substrate due to its structural stability under the given synthetic conditions of the inorganic semiconductor nanostructures. The developed material was characterized by means of scanning transmission electron microscopy with energy dispersive X-ray spectroscopy (STEM EDX) mapping, X-ray photoelectron spectroscopy (XPS), scanning electron microscopy (SEM), Fourier transform infrared (FT-IR), X-ray diffraction (XRD), Brunauer−Emmett−Teller (BET) surface analysis, and X-ray diffraction. The controlled growth of $Bi_4O_5Br_2$/BiOBr on a cellulose membrane (CM) enables a thin coating on the mechanically stable membrane and shows faster degradation of RhB than on pure $Bi_4O_5Br_2$/BiOBr photocatalyst. The removal of inorganic pollutants, such as Co(II) and Ni(II), which are also of high importance in Li-ion battery recycling, on the CM/$Bi_4O_5Br_2$/BiOBr composite was investigated with respect to its kinetic parameters.

EXPERIMENTAL SECTION

Materials. Bismuth(III) nitrate pentahydrate ($Bi(NO_3)_3$ $5H_2O$), 98%, Alfa Aesar), potassium bromide (KBr, ACS), sodium hydroxide (NaOH, 98−100.5%, Honeywell, Charlotte, NC, long pine fibers from MetsäBoard and commercial grade microfibrillated cellulose (MFC) Exilva 01-V supplied as 10 wt % suspensions from Borregard, Norway, were used for the production of the membranes. Pine fibers had a diameter of 25−30 mm and the MFC had diameters within the range of 10−100 nm. Nickel(II) nitrate hexahydrate (Puratronic 99.9985 wt %) and cobalt(II) nitrate hexahydrate (Puratronic 99.999 wt %) were purchased from Alfa Aesar. RhB (analytical standard) was purchased from Sigma.

Synthesis of Cellulose Membrane (CM). Cellulose membrane was produced in continuous mode using Experimental Paper Machine (XPM) pilot at MoRe Research, Örnsköldsvik, Sweden.[55] Hybrid suspension of microfibrillated cellulose with long pine fibers (softwood pulp) was prepared in the machine chest and then pumped into machine headbox to produce composite membranes. Machine speed was same (1.4 m/min) and density of fabricated composite membranes was targeted to 60 g/m^2. The composite membranes of 5 × 1 m in dimensions were prepared using the XPM machine. The mechanical properties are summarized in Supporting Information (SI) Table S1.

Synthesis of $Bi_4O_5Br_2$/BiOBr. We dissolved 20.6 mmol of $Bi(NO_3)_3$ and 16.8 mmol of KBr in 10 mL of DI water, and then 1 M of NaOH was added dropwise to the solution until pH 13. The resulting solution was transferred into a 20 mL Teflon-lined stainless-steel autoclave filled up to 80% of the total volume followed by a hydrothermal treatment at 115 °C for 20 h. After the reaction, the reactor was cooled to room temperature to collect the precipitate and washed with DI water until pH 7 was reached.

Synthesis of CM/$Bi_4O_5Br_2$/BiOBr. 20.6 mM of $Bi(NO_3)_3$. H_2O and 16.8 mM of KBr were dissolved in 10 mL of DI water, and then 1 M of NaOH was added dropwise to the solution to pH 13. The basic conditions are required for the hydrothermal synthesis of the semiconductor nanostructures. Strongly acidic conditions are not suitable due to potential decomposition of cellulose. Fragment (5 × 3 cm) of cellulose membrane was added to the solution. The latter was transferred into a 20 mL Teflon-lined stainless-steel autoclave filled up to 80% of the total volume followed by a hydrothermal treatment at 115 °C for 20 h. After the reaction, the reactor was cooled to room temperature to collect the precipitate and washed with DI water until pH 7 was observed.

FT-IR Spectroscopy and Powder XRD. FT-IR spectra were carried out using a Varian 610-IR FT-IR spectrometer. The X-ray diffraction (XRD) pattern was determined on a Panalytical X'Pert Alpha1 using Cu K_α (λ = 1.5406 Å) radiation in the 2θ range from 10 to 80°.

Electron Microscopy. The morphology was evaluated using electron diffraction and high-resolution transmission electron microscopy on a JEOL 2100F operated at 200 kV, while elemental information was acquired using EDX on an aberration-corrected Themis Z (Thermo Fisher) operated at 300 kV. The topography was evaluated using SEM JEOL JSM-7000F. Thermal stability was

https://dx.doi.org/10.1021/acsami.0c12739
ACS Appl. Mater. Interfaces 2020, 12, 42891−42901

evaluated using thermogravimetric analysis (TGA) in a PerkinElmer TGA 7 thermobalance.

XPS. Measurements were performed on a Theta Probe (Thermo Fisher Scientific) System. The X-ray source was a monochromated Al K_α source at 1386.6 eV. The spectrometer was calibrated to 368.21 eV binding energy (BE) of the Ag $3d_{5/2}$ line for metallic silver and the linearity was corrected to BE of 932.62 eV for the Cu $2p_{3/2}$ line and 83.96 eV for the Au $4f_{7/2}$ line. Charge compensation was done using a flood gun for low-energy electrons and argon ions at 1 eV. The binding energy scale was calibrated using the C 1s component at 285.0 eV (typical of C−C).

Specific Surface Area and Pore Size Distributions. Specific surface area and pore volume were determined from nitrogen adsorption/desorption isotherms at 77 K (Micromeritics ASAP 2020 sorption analyzer). The samples were degassed at 80 °C before the measurements. The pore size distributions (PSD) were calculated using Barret-Joyner-Halenda (BJH) method.

Point of Zero Charge Determination. In order to measure pH_{PZC} values in sequential order of coprecipitation process after each surface modification, pH drift method was applied. pH drift was chosen over other conventional methods, such as titrations because it is less time-consuming, results are available in few steps using regular laboratory apparatuses which indeed lower the overall expenditure of the experiment, and the result obtained from this method is in line with the ones obtained from other applied methods.[56,57] According to this method, solutions of 0.01 mol L^{-1} NaCl in 10 mL flask were adjusted to pH values of 2−10 ($pH_{initial}$) using 0.05 mol L^{-1} NaOH and 0.05 mol L^{-1} HCl. After which, 5 mg of CM/$Bi_4O_5Br_2$/BiOBr was added to the flask and shaken at 180 rpm for 24 h. Then, the final pH (pH_e) of the samples were measured using a pH meter and plotted against initial pH. The point of intersection (point zero) of the resulting plot with the line passing origin (pH_e−$pH_{initial}$) gives pH_{PZC}.[58]

Photocatalytic Dye Degradation. A RhB solution of 8 mg·L^{-1} in DI water and 0.013 M of hydrogen peroxide was prepared. For the photocatalytic tests, the CM/$Bi_4O_5Br_2$/BiOBr hybrid membrane was added to the solution and this mixture was irradiated with blue light 405 nm (20 W) light source. Subsequently, another photocatalytic test was performed with the mass of the inorganic semiconductor $Bi_4O_5Br_2$/BiOBr, which was determined to be 17 mg from the thermal analysis (vide infra). The photocatalytic tests were carried out in darkness in order to avoid any other irradiation on the sample; therefore, only the light from the lamp could reach the sample. At 20 min intervals, 5 mL aliquots were taken from the solution for analysis. The absorption of these aliquots was taken at different intervals using a spectrometer. The absorbance value obtained were then converted to mg·L^{-1}, and the observed concentrations were plotted against time to give the degradation rate.

Batch Adsorption of Co(II) and Ni(II) Ions. Cellulose membrane (CM) and CM/Bi_4O_5Br/BiOBr materials were tested and compared as feasible sorbents for heavy metal ions removal from aqueous solutions. For this study, we have decided to investigate the adsorption ability of our material toward Co(II) and Ni(II) ions, due to their hazardous nature for humans and environment.[59] The adsorption kinetics for solutions of Co(II) and Ni(II) were measured using a static method. The batch adsorption experiments were performed by shaking 0.03 g of the cellulose membrane or modified cellulose membrane in flasks containing 25 mL solutions of Co(II) or Ni(II) with the concentration of 20 mg·L^{-1} and 50 mg·L^{-1}. The flasks were shaken in a Heidolph Unimax 1010 incubating shaker (Germany) for 5, 24, 48, 72, and 94 h at 180 rpm and 22 °C. After that, the solutions were separated from the sorbents by filtration and the final concentration of metal ions was determined photometrically.[60] The absorbance was measured using a UV-3100PC spectrophotometer (VWR, Radnor, PA), by complexing Co(II) ions with 4-(2′-pirydylazo)resorcinol (at the wavelength of 500 nm) and Ni(II) ions with dimethylglyoxime (at 470 nm). To obtain high accuracy of the measurements, each sample was determined three times and the obtained results were taken as mean value. The adsorption capacity (q_e) for each sorbent was calculated according to the following equation:

$$q_e = \frac{(c_0 - c_e)V}{m} \quad (1)$$

where c_0 and c_e are the initial and equilibrium concentration of metal ions respectively (mg·L^{-1}), V is the volume of the sample (L) and m is the sorbent mass (g).

The removal efficiency (R) was calculated using the formula:

$$R = \frac{(c_0 - c_e)}{c_0} \cdot 100\% \quad (2)$$

where C_0 and C_e are the initial and equilibrium concentration of metal ions respectively (mg·L^{-1}). The pseudo-first and pseudo-second-order equations were applied to kinetics analysis of Co(II) and Ni(II) ions adsorption on the membranes. The pseudo-first-order equation:[61,62]

$$\log(q_e - q_t) = \log q_{e-}\frac{kt}{2.303} \quad (3)$$

The pseudo-second-order equation:[63]

$$\frac{t}{q_t} = \frac{1}{k_2 q_e^2} + \frac{t}{q_e} \quad (4)$$

where, q_e and q_t are the amounts of metal adsorbed (mg·g^{-1}) at equilibrium time and at any instant of time t, K_1 (1·min^{-1}) is the rate constant of the pseudo-first-order adsorption and K_2 (g·mg^{-1}·min^{-1}) is the pseudo-second-order rate constant.

RESULTS AND DISCUSSION

Structural Characterization. The identification and purity of inorganic component, i.e., the synthesis with no inserted CM substrate in the autoclave, was performed by means of XRD (Figure 1). The XRD patterns show presence of

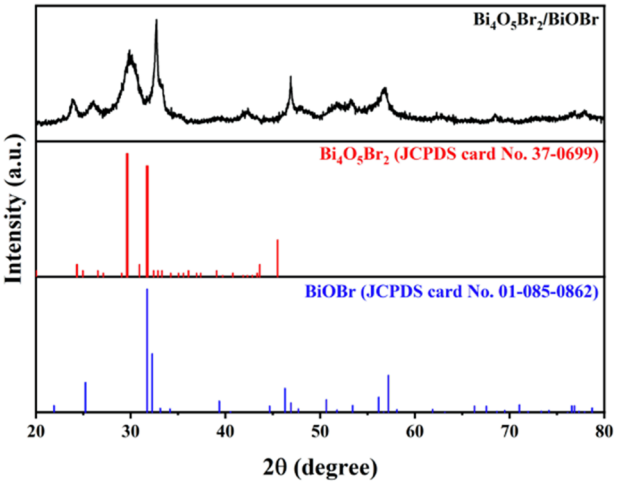

Figure 1. Comparison of experimental and simulated PXRD patterns of synthesized photocatalyst without nanocellulose. The simulated patterns were indexed for BiOBr and $Bi_4O_5Br_2$ by using the crystallographic data from JCPDS-01-085-0862 and JCPDS-37-0699.

two ternary phases $Bi_4O_5Br_2$[64] and BiOBr[65] in the synthesized material at described reaction conditions. Obtained nanosheets differ from previously reported where photocatalytic activity has been evaluated for $Bi_4O_5Br_2$ nanostructures.[24,30,66] We did not attempt to obtain one of these phases as single-phase materials by increasing the reaction temperature due to possible changes in functionalization character of cellulose carrier. The original CM consists of intergrown fibers that

https://dx.doi.org/10.1021/acsami.0c12739
ACS Appl. Mater. Interfaces 2020, 12, 42891−42901

build up the macroscopic object (Figure 2a,b). Upon hydrothermal growth of the $Bi_4O_5Br_2$/BiOBr photocatalyst

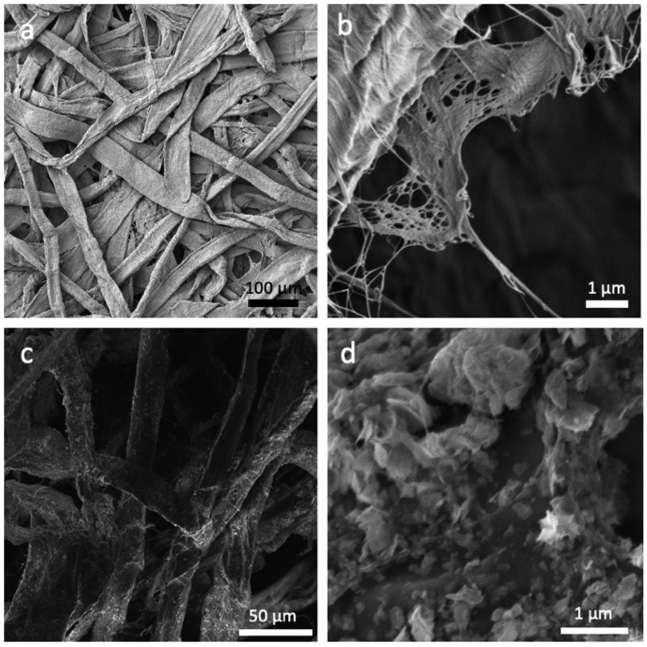

Figure 2. SEM micrographs of (a,b) pristine CM and (c,d) hybrid membranes CM/$Bi_4O_5Br_2$/BiOBr.

on the CM, changes on surface of the CM are observed (Figure 2c). The collected SEM micrograph at higher magnification shows the bioinorganic interface, i.e., successful functionalization of the CM with the photocatalyst in the form of two-dimensional nanostructure which are stacked to each other (Figure 2d). After hydrothermal growth, the CM/$Bi_4O_5Br_2$/BiOBr sample demonstrates mechanical stability and was used for photocatalytic characterization and for adsorption processes.

Figure 3 summarizes the complementary TEM analysis performed for the $Bi_4O_5Br_2$/BiOBr nanosheets (Figure 3a–c) and the CM/$Bi_4O_5Br_2$/BiOBr (Figure 3d–h). The obtained $Bi_4O_5Br_2$/BiOBr product contains a monodisperse mixture of crystalline nanosheets with an average size of 10 nm. The inset in Figure 3a shows the HRTEM image of the nanosheets at higher magnification. However, for the pristine nanosheets, selected area diffraction patterns (SAED) in Figures 3b,c show that BiOBr is the dominant phase. Figure 3d,e depicts a clear morphology of cellulose with supported nanosheets $Bi_4O_5Br_2$/BiOBr and the corresponding SAED patterns confirm the mixed phase, which is in agreement with the PXRD patterns (vide supra). The results of the EDX analysis of CM/$Bi_4O_5Br_2$/BiOBr is presented in Figure 3f–h. These data were acquired in scanning TEM (STEM) mode under moderately low-dose conditions (estimated to be 60 e^-/Å for this data set) to minimize any potential beam damage. The left-most panel labeled "HAADF survey" presents an overview micrograph of an agglomerate containing suspected strands of cellulose that is coated with $Bi_4O_5Br_2$/BiOBr. The use of the high-angle annular dark field (HAADF) detector results in a mass–thickness contrast. The yellow box denotes the exact region scanned for EDX analysis, and the subsequent HAADF scan is presented in the second panel. It is possible to observe individual lattice fringes in the cellulose in this image, allowing

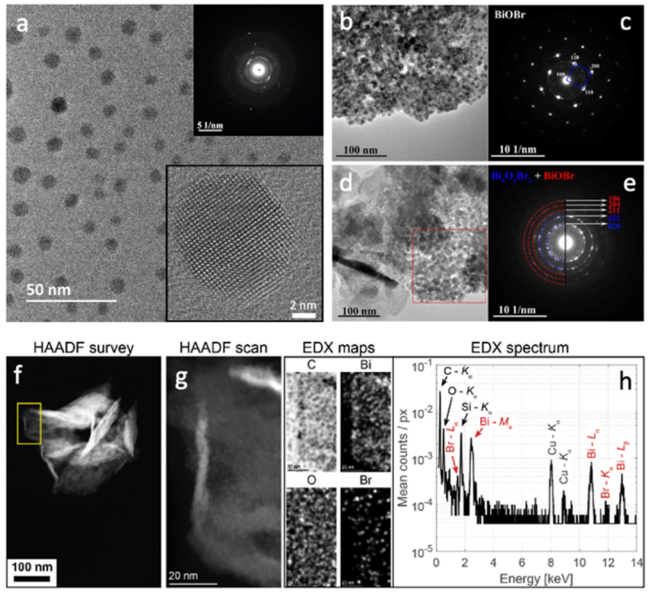

Figure 3. (a) Overview TEM image of $Bi_4O_5Br_2$/BiOBr nanosheets. The inset shows a high magnification of the nanosheets in the ED patterns. (b,c) TEM images and corresponding SAED patterns for $Bi_4O_5Br_2$/BiOBr nanosheets and (d-e) CM/$Bi_4O_5Br_2$/BiOBr. (f) HAADF survey of CM/$Bi_4O_5Br_2$/BiOBr and (g) selected area for elemental mapping. Note the cellulose fiber wrapped within agglomerated sheets of the inorganic counterpart. (h) STEM EDX elemental map for CM/$Bi_4O_5Br_2$/BiOBr.

us to confirm its presence. The EDX maps for C, O, Br, and Bi are presented in the next panel. Due to the very low probe current, these maps contain very few counts. An estimate for the missing counts was obtained by employing a strong smoothness assumption; the spectral dimension of the acquired hyperspectral datacube was convolved with a Gaussian kernel (fwhm: 2 energy channels) prior to integration under the EDX peaks. The resulting maps were additionally blurred along their spatial dimensions. Although this results in a strong degradation of the energy and spatial resolution, the Bi and Br signals are clearly localized to the agglomerate, with a strong Bi contribution along the cellulose wires. In the final panel, the average EDX spectrum from each pixel within the agglomerate region is presented along with elemental labels. The peaks corresponding to O, Bi, and Br are clearly distinguishable. The C peaks originate from the support film, the Cu peaks arise from the use of a copper TEM grid, and Si is an impurity introduced during the preparation of the TEM sample for analysis. The exceedingly low count rate is highlighted by these very low average values.

The surface composition of the CM/$Bi_4O_5Br_2$/BiOBr sample was determined by the XPS technique (Figure 4). In the XPS C 1s spectrum, four components can be distinguished at 285.0 eV (C–C), 286.8 eV (C–OH), 288.2 eV (O–C–O and C═O), and 289.5 eV (O–C═O).[67] The most intensive signal corresponds to C–O and O–C–O from the glucose units of cellulose, and the other states probably form as a side product or contaminant. This proves that the synthetic conditions at relatively low temperature enables to maintain the carboxylic groups of cellulose and, consequently, its surface functionality (vide infra). Analysis of Bi 4f shows the presence of three different states of Bi: two of them are related to bismuth oxybromides ($Bi_4O_5Br_2$/BiOBr) and additional Bi^{5+} states on the CM/$Bi_4O_5Br_2$/BiOBr surface. The obtained

https://dx.doi.org/10.1021/acsami.0c12739
ACS Appl. Mater. Interfaces 2020, 12, 42891–42901

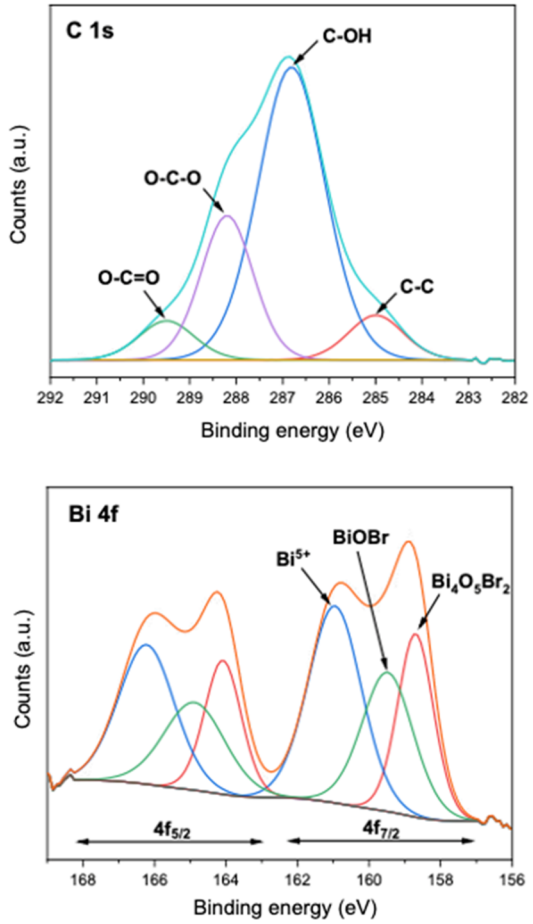

Figure 4. XP spectra of CM/$Bi_4O_5Br_2$/BiOBr membrane. The C 1s spectrum corresponds to the cellulose and the functional groups.

results are in good agreement with the XRD analysis, where the presence of $Bi_4O_5Br_2$ and BiOBr phases has been confirmed. $Bi_4O_5Br_2$ is manifested by the doublet at 158.7 eV ($4f_{7/2}$) and 164.1 eV ($4f_{5/2}$), whereas BiOBr is confirmed by the photoemission at 159.5 eV ($4f_{7/2}$) and 164.9 eV ($4f_{5/2}$).[68,69] The difference in binding energies of Bi $4f_{7/2}$ peaks for both phases is calculated to be 0.8 eV, clearly confirming the various chemical environments of Bi^{3+}. Furthermore, in the measured sample, additional Bi 4f components (at 161.0 eV − $4f_{7/2}$ and 166.2 eV − $4f_{5/2}$) are observed. Such high binding energy values suggest the existence of Bi in pentavalent form within the surface region, which shows lower kinetic energy of emitted photoelectrons compared to Bi^{3+} due to larger Coulomb attraction.[70,71]

FT-IR analysis was performed to identify the functional groups of the CM/$Bi_4O_5Br_2$/BiOBr composites (Figure 5). A broad band in the range of 3666−3000 cm^{-1} corresponds to the stretching vibrations of hydroxyl groups (O−H), whereas the band at 2896 cm^{-1} is associated with C−H stretching.[14] The absorption band at 1643 cm^{-1} corresponds to the O−H bending of adsorbed water in cellulose.[72] The bands at 1428 and 1317 cm^{-1} were attributed to CH_2 wagging and CH_2 symmetric bending respectively, in the cellulose membrane molecular structure.[73] The band at 1159 cm^{-1} is related to C−O antisymmetric stretching and the sharp band at 1027 cm^{-1} corresponds to C−O and C−C stretching. The absorption band at 892 cm^{-1} is known for C−O−C stretching at β-linked glucose of cellulose.[74] The amount of the photocatalyst on the

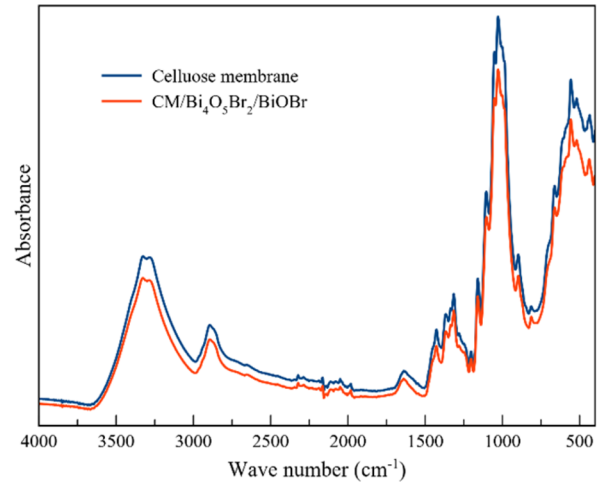

Figure 5. FTIR spectrum of CM and CM/$Bi_4O_5Br_2$/BiOBr. Both samples were measured after photocatalytic experiments.

CM surface was determined by thermal analysis (Figure 6). The TG curve of CM/$Bi_4O_5Br_2$/BiOBr was collected in the

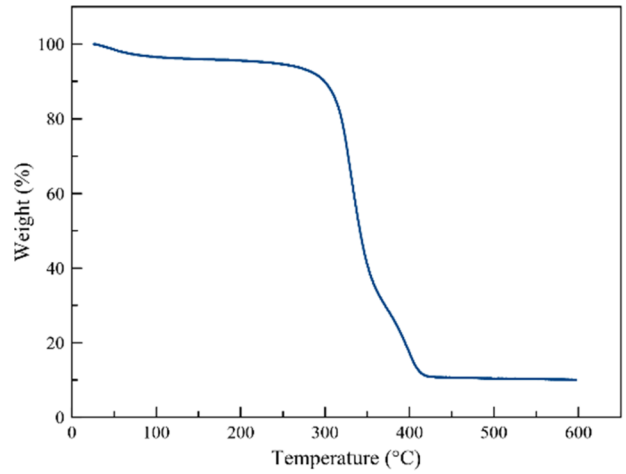

Figure 6. TGA curve of CM/$Bi_4O_5Br_2$/BiOBr in air. The weight loss above 370 °C is due to thermal decomposition of cellulose.

temperature range from 100−700 °C. The weight loss above 100 °C is connected to evaporation of adsorbed water and the subsequent weight loss starting 370 °C corresponds to the decomposition of cellulose.[75] From the TG analysis, the mass of the $Bi_4O_5Br_2$/BiOBr coating on cellulose was determined to be 11 wt %. The BET surface area was found to be 0.9 $m^2 \cdot g^{-1}$ for unmodified membrane with a slight increase for cellulose membrane with immobilized catalyst to 1.8 $m^2 \cdot g^{-1}$. Since the surface charge for given pH range is a decisive parameter for potential sorbent capacity, the pH drift method was applied for the CM/$Bi_4O_5Br_2$/BiOBr composite. In this method, samples were dispersed in low ionic strength aqueous media and after equilibration, the drift in pH values were recorded in order to calculate the pH_{PZC}. Figure 7 illustrates the obtained curve for CM/$Bi_4O_5Br_2$/BiOBr with a pH_{PZC} value of 3.9. This indicates that above this pH value, the material is suitable for adsorption of metal ions; even upon modification with the photocatalyst for dye degradation.

Dual Functionality for Removal of Inorganic and Organic Pollutants. *Photocatalytic Degradation of RhB.*

https://dx.doi.org/10.1021/acsami.0c12739
ACS Appl. Mater. Interfaces 2020, 12, 42891−42901

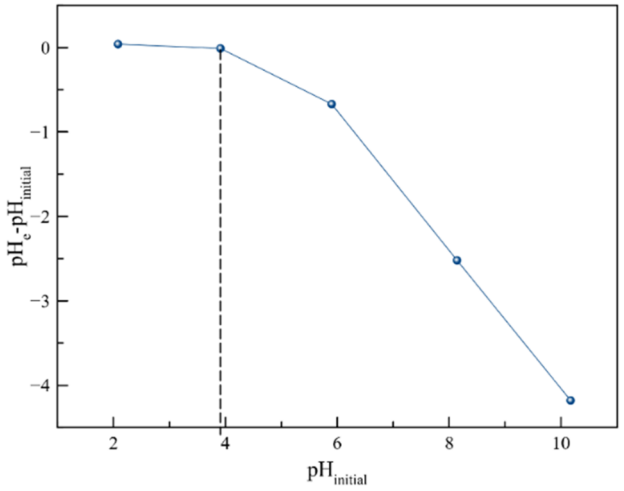

Figure 7. PH_{pzc} of the bioinorganic composite CM/$Bi_4O_5Br_2$/BiOBr. The material exhibits a negative surface charge above pH 4.

Figure 8 depicts the results of photocatalytic degradation of RhB as a function of time under illumination with a 405 nm

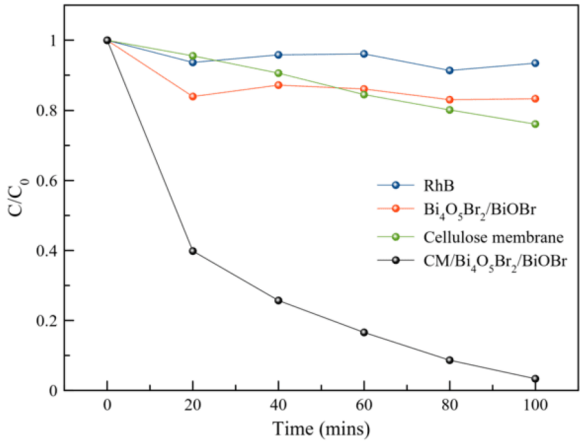

Figure 8. Photocatalytic degradation of RhB. Experiments were carried out under 405 nm illumination (20 W) with addition of hydrogen peroxide. The loading of the semiconducting photocatalyst (red curve) was 17 mg; being the same as for the CM/$Bi_4O_5Br_2$/BiOBr sample.

(20 W) lamp. The amount of the photocatalyst, being equal 17 mg (red curve), was determined by thermogravimetric analysis to ensure equal parameters for comparison. Consequently, the decay of the dye concentration could be improved if higher catalyst loading, i.e., higher surface area of the CM/$Bi_4O_5Br_2$/BiOBr composite, would be used. The blue curve represents the baseline for the photocatalytic degradation and was recorded without the presence of the membranes. The pure cellulose membrane slightly decreases the concentration of the dye in solution, which is not an unexpected observation due to the known sorption capacity of cellulose toward organic substances. This decrease in RhB concentration is almost equal to the dye degradation on the bare $Bi_4O_5Br_2$/BiOBr photocatalyst. When comparing these performances to the CM/$Bi_4O_5Br_2$/BiOBr, a synergistic effect between the CM and inorganic semiconductor constituents can be observed. The bioinorganic composite shows superior performance in comparison to its individual constituents, while maintaining its second functionality as potential sorbent material for removal of positively charged entities. Scheme 1 illustrates the

Scheme 1. Schematic Illustration of Charge Separation at the BiOBr/$Bi_4O_5Br_2$ type-II Heterojunction upon Illumination[a]

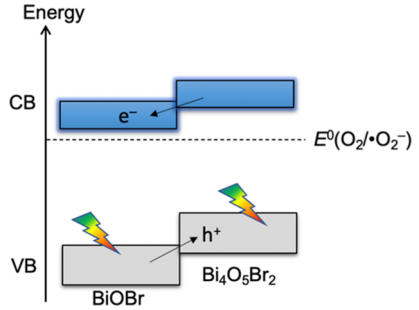

[a]The different positions of conduction band (CB) and valence band (VB) edges decrease electron-hole recombination. RhB can be either decomposed by the photogenerated holes or oxygen-radicals.

band alignment of the heterojunction and suggested mechanism for photocatalytic RhB degradation. The augmented photocatalytic behavior can be attributed to minimized agglomeration of the nanosheets, i.e., minimized loss of photochemically exposed surface area. Since the photocatalytic performance depends on the power and wavelength of the used illumination source, a direct comparison to other semiconductor systems on membranes is not possible at the moment. However, the application of the cellulose membrane as one parameter in the photocatalytic system strongly increases the photochemical response.

Adsorption of Co(II) and Ni(II) Ions. Both CM and CM/$Bi_4O_5Br_2$/BiOBr composite were tested for adsorption of Co(II) and Ni(II) ions. The CM/$Bi_4O_5Br_2$/BiOBr composite unifies the mechanical stability and easy manufacturing of cellulose membranes for sorption of metal ions.[76−79] The adsorption rate provides crucial information on efficiency of adsorbent material and the possibility to use it on a large scale. Therefore, we investigated the influence of phases contact time on the adsorption efficiency of membranes before and after catalyst immobilization with respect to Co(II) and Ni(II) ions. For that, bivalent metal ions solutions were adsorbed from aqueous solutions with initial concentration 20 mg·L^{-1} and 50 mg·L^{-1} by modified and unmodified membranes in the neutral media during 5 h, 24 h, 48 h, 72 h, and 96 h in order to reach an removal efficiency close to 100%. The dependency of phase contact time for Co(II) and Ni(II) ions adsorption on CM and CM/$Bi_4O_5Br_2$/BiOBr on removal efficiency is presented in Figure 9.

It can be seen that 70−80% of Co(II) ions could be adsorbed during the first 5 h of contact with metal solutions of initial concentration of 20 mg·L^{-1} and 50 mg·L^{-1}. In the case of Ni(II) ions, the adsorption occurs more slowly, i.e., during the same time it is possible to remove 47.5−48.0% of the Ni(II) ions from solutions with initial concentration of 20 mg·L^{-1} by both membranes. For higher initial concentration of Ni(II) (50 mg·L^{-1}), the removal efficiency was found to be 50.9% and 58.7% for CM and CM/$Bi_4O_5Br_2$/BiOBr, respectively. The removal efficiency toward both metals increased slowly up to 94−100% during 5−96 h. Based on experimental data the adsorption capacity toward Co(II) was

https://dx.doi.org/10.1021/acsami.0c12739
ACS Appl. Mater. Interfaces 2020, 12, 42891−42901

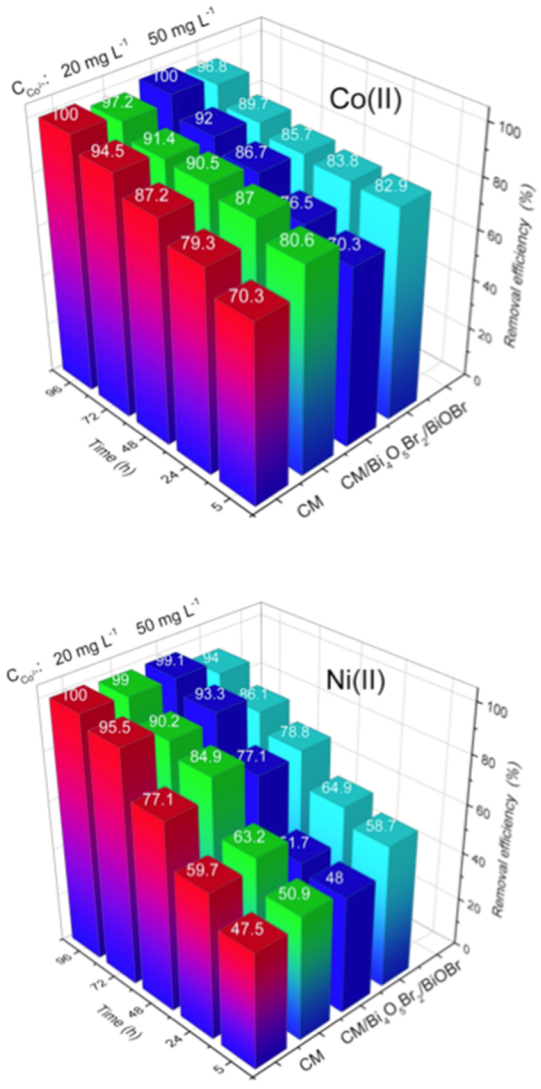

Figure 9. Influence of phase contact time on Co(II) and Ni(II) ions adsorption using CM and CM/$Bi_4O_5Br_2$/BiOBr composites.

28.7 mg·g^{-1} for CM and 37.3 mg·g^{-1} for CM/$Bi_4O_5Br_2$/BiOBr; toward Ni(II): 29.7 mg·g^{-1} for CM and 30.2 mg·g^{-1} for CM/$Bi_4O_5Br_2$/BiOBr. Thus, CM/$Bi_4O_5Br_2$/BiOBr showed higher affinity to Co(II) ions than to the Ni(II) ions from diluted solutions (20−50 mg·L^{-1}). We recently demonstrated on mesoporous SiO_2 with grafted carboxylic groups which achieve an adsorption capacity toward Co(II) and Ni(II) 166 mg·g^{-1} and 172 mg·g^{-1}.[82] These values are among the highest capacities reported for both cations. However, a direct comparison is difficult, because the cellulose membranes had a much smaller surface area and could be easily processed in industrial application. On the other side mesoporous powders, despite higher surface area and thus higher adsorption capacity, require more complex engineering solutions. The advantage of the *Celluphot* concept over conventional sorbents is the integration of heterojunction semiconductor nanosheets on cellulose, while maintaining the structural features that are required for adsorption.

The kinetics of adsorption of Co(II) and Ni(II) ions on the membranes was studied by application of pseudo-first and pseudo-second-order equations in order to understand the mechanisms of adsorption and the rate-controlling step of the process (Figure 10). The parameters were calculated from the fitting of experimental data with applied kinetic models (Table 1). The linear relationship and high values of correlation

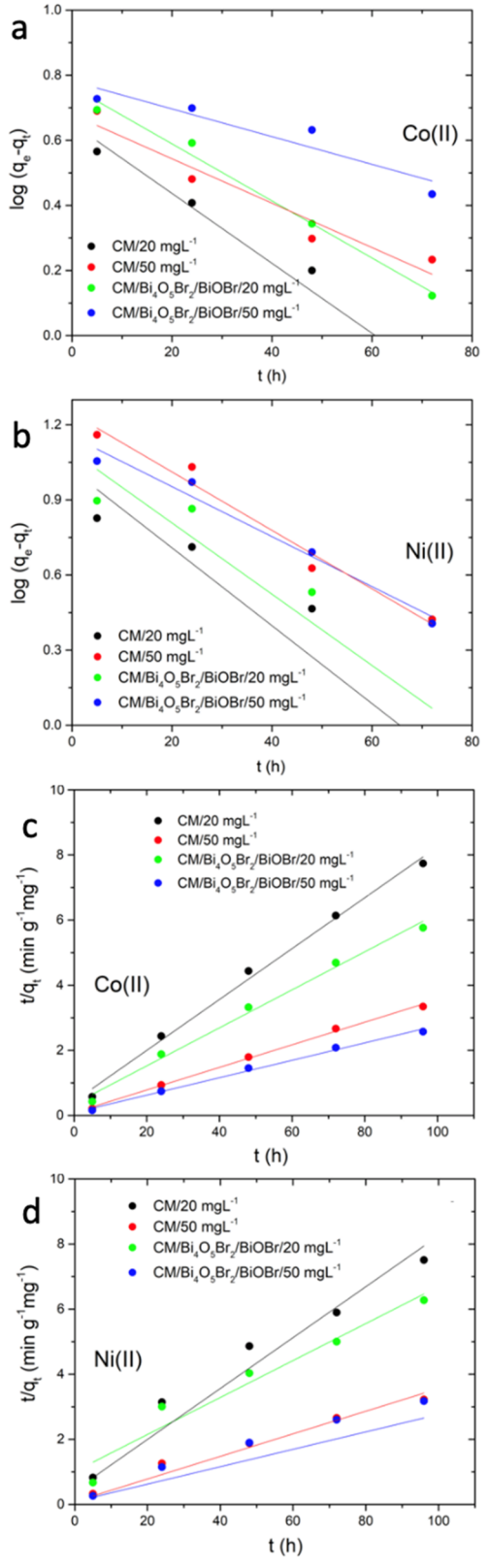

Figure 10. Pseudo-first order plots and pseudo-second-order plots for Co(II) and Ni(II) ions adsorption kinetics by CM and CM/$Bi_4O_5Br_2$/BiOBr membranes.

https://dx.doi.org/10.1021/acsami.0c12739
ACS Appl. Mater. Interfaces 2020, 12, 42891−42901

Table 1. Kinetic Parameters for the Adsorption of Co(II) and Ni(II) Ions on the CM and CM/$Bi_4O_5Br_2$/BiOBr Membranes

		Co(II)		Ni(II)	
kinetics model	parameter symbol, unit	20 mg·L^{-1}	50 mg·L^{-1}	20 mg·L^{-1}	50 mg·L^{-1}
CM					
pseudo-first order	qe, $_{cal}$, mg·g^{-1}	4.49	4.78	10.47	17.60
	K_1, 1·min^{-1}	0.025	0.016	0.036	0.027
	R^2	0.9756	0.9350	0.8917	0.9752
pseudo-second order	q_e, cal, mg·g^{-1}	12.79	28.82	14.37	32.15
	K_2, g·mg^{-1}·min^{-1}	0.014	0.014	0.005	0.003
	R^2	0.9942	0.9974	0.9694	0.9851
CM/$Bi_4O_5Br_2$/BiOBr					
pseudo-first order	q_e, cal, mg·g^{-1}	5.82	6.05	12.39	14.22
	K_1, 1·min^{-1}	0.020	0.010	0.033	0.023
	R^2	0.9884	0.8833	0.9026	0.9743
pseudo-second order	q_e, cal, mg·g^{-1}	17.12	37.45	17.61	31.75
	K_2, g·mg^{-1}·min^{-1}	0.010	0.008	0.004	0.003
	R^2	0.9694	0.9851	0.9490	0.9864

coefficients (R^2 = 0.95−0.99) confirm that the pseudo-second-order equation kinetic model fits well experimental data and is suitable for description of the kinetics of Co(II) and Ni(II) ion removal on both modified and unmodified membranes. These results indicate that the adsorption capacity of the CM membrane is independent of the coating with the photocatalyst. The adsorption mechanism of the metal ions on the cellulose surface may be attributed to the presence of carboxylic groups on the surface; as evidenced based on the XPS analysis. Increasing the initial metals concentration from 20 to 50 mg·L^{-1} caused a slight decrease of adsorption rate for all systems. The rate of adsorption was found to be higher for the systems CM/Co(II): 0.014 g·mg^{-1}·min^{-1}, and CM/$Bi_4O_5Br_2$/BiOBr/Co(II): 0.010−0.008 g·mg^{-1}·min^{-1}, than for the same systems with Ni(II) ions: 0.005−0.003 g·mg^{-1}·min^{-1}. Since the first adsorption step was found to be relatively fast with high percentage of removal of selected metals from initial solutions (20 and 50 mg·L^{-1}) it could be concluded that the membranes with immobilized catalyst could be applied in a large scale where fast and effective adsorption of metals are required.

These results indicate a high potential of the CM/$Bi_4O_5Br_2$/BiOBr composite for heavy metal recovery from wastewater; even with the decrease of sorption capacity for metal ions compared to pure CM was observed. Although metal ions can be desorbed in highly acidic environments (pH 1), it is generally known that cellulose exhibits under acidic conditions a structural instability of the surface groups. By combining photocatalytic properties of $Bi_xO_yBr_z$ compounds with sorption ability of cellulose membrane, we end up with a promising material for simultaneous adsorption and photodegradation for wastewater purification from heavy metals and organic dyes. Further progress may be expected for cellulose nanofibers obtained by electrospinning due to higher specific surface area.[80,81] Since the adsorption of Co^{2+} and Ni^{2+} cations is determined by the electrostatic interaction with the functional groups,[82] i.e., carboxylic and/or hydroxylic group, of cellulose, an increased specific surface area could increase the adsorption capacity.

CONCLUSION

We have demonstrated the fabrication of a bioinorganic membrane based on cellulose and $Bi_4O_5Br_2$/BiOBr nanosheets, which can remove both inorganic and organic pollutants by two complementary mechanisms. The biomaterial in form of cellulose ensures the mechanical stability of the membrane and can adsorb metal ions. The composite can adsorb both Co(II) and Ni(II) ions and our kinetic study confirmed that the pseudo-second equation kinetic model fits well experimental data and is suitable for description of the kinetics of Co(II) and Ni(II) ions on both modified and unmodified membranes. The controlled growth of the inorganic semiconducting nanosheets directly on the cellulose fibers enables photocatalytic decomposition of organic dyes, which has been shown on the example of RhB. The bioinorganic composite CM/$Bi_4O_5Br_2$/BiOBr shows a synergistic effect in the photocatalytic dye degradation, because it exceeds the removal efficiency of its single constituents. The direct hydrothermal growth at 115 °C of the semiconductor nanosheets on cellulose (nano)fibers enables to fabricate thin photochemically active coatings while preserving the kinetic mechanism of metal ion adsorption on the carboxylic groups of the biosubstrate. The fabrication of the bioinorganic interface at the nanoscale was confirmed by both SEM and STEM EDX mapping.

The critical advancement of our work is the controlled formation of the bioinorganic interface between cellulose and nanosheets of the ternary Bi−O−Br system, which enables to produce materials with dual functionality. Beyond the scope of water purification and given the applications of semiconductors within the ternary Bi−O−Br system, the hybrid material may be also an attractive candidate for a plethora of photocatalytic reactions.

ASSOCIATED CONTENT

Supporting Information

The Supporting Information is available free of charge at https://pubs.acs.org/doi/10.1021/acsami.0c12739.

Mechanical properties of cellulose membrane; SEM image of $Bi_4O_5Br_2$/BiOBr sample without cellulose substrate (PDF)

AUTHOR INFORMATION

Corresponding Authors

Adam Slabon − *Department of Materials and Environmental Chemistry, Stockholm University, 106 91 Stockholm, Sweden;* orcid.org/0000-0002-4452-1831; Email: adam.slabon@mmk.su.se

Aji P. Mathew − *Department of Materials and Environmental Chemistry, Stockholm University, 106 91 Stockholm, Sweden;* orcid.org/0000-0001-8909-3554; Email: aji.mathew@mmk.su.se

Authors

Joy Onwumere − *Department of Materials and Environmental Chemistry, Stockholm University, 106 91 Stockholm, Sweden;* orcid.org/0000-0002-6889-0527

https://dx.doi.org/10.1021/acsami.0c12739
ACS Appl. Mater. Interfaces 2020, 12, 42891−42901

Jędrzej Piątek − *Department of Materials and Environmental Chemistry, Stockholm University, 106 91 Stockholm, Sweden;* orcid.org/0000-0002-1429-4586
Tetyana Budnyak − *Department of Materials and Environmental Chemistry, Stockholm University, 106 91 Stockholm, Sweden;* orcid.org/0000-0003-2112-9308
Jianhong Chen − *Department of Materials and Environmental Chemistry, Stockholm University, 106 91 Stockholm, Sweden;* orcid.org/0000-0001-9020-1786
Serhiy Budnyk − *AC2T research GmbH, 2700 Wiener Neustadt, Austria*
Zoheb Karim − *MoRe Research Örnsköldsvik AB, SE-89122 Örnsköldsvik, Sweden;* orcid.org/0000-0002-4196-8419
Thomas Thersleff − *Department of Materials and Environmental Chemistry, Stockholm University, 106 91 Stockholm, Sweden;* orcid.org/0000-0002-0999-3569
Piotr Kuśtrowski − *Faculty of Chemistry, Jagiellonian University, 30-387 Kraków, Poland;* orcid.org/0000-0001-8496-0559

Complete contact information is available at: https://pubs.acs.org/10.1021/acsami.0c12739

Author Contributions

All authors have given approval to the final version of the manuscript.

Notes

The authors declare no competing financial interest.

■ ACKNOWLEDGMENTS

A.S., A.P.M., S.B., J.O., and J.P. are thankful for financial support from MISTRA (project: *SafeChem*). P.K. acknowledges the European Regional Development Fund in the framework of the Polish Innovation Operational Program (contract no. POIG.02.01.00-12-023/08) for financial support. T.T. acknowledges support from the Swedish Research Council (project no. 2016-05113).

■ REFERENCES

(1) Nirumand, L.; Farhadi, S.; Zabardasti, A.; Khataee, A. Synthesis and Sonocatalytic Performance of a Ternary Magnetic MIL-101(Cr)/RGO/$ZnFe_2O_4$ Nanocomposite for Degradation of Dye Pollutants. *Ultrason. Sonochem.* **2018**, *42*, 647−658.
(2) Mohamed, A.; El-Sayed, R.; Osman, T. A.; Toprak, M. S.; Muhammed, M.; Uheida, A. Composite Nanofibers for Highly Efficient Photocatalytic Degradation of Organic Dyes from Contaminated Water. *Environ. Res.* **2016**, *145*, 18−25.
(3) Navarro, P.; Gabaldón, J. A.; Gómez-López, V. M. Degradation of an Azo Dye by a Fast and Innovative Pulsed Light/H2O2 Advanced Oxidation Process. *Dyes Pigm.* **2017**, *136*, 887−892.
(4) Alvi, M. A.; Al-Ghamdi, A. A.; ShaheerAkhtar, M. Synthesis of ZnO Nanostructures via Low Temperature Solution Process for Photocatalytic Degradation of Rhodamine B Dye. *Mater. Lett.* **2017**, *204*, 12−15.
(5) Anastopoulos, I.; Hosseini-Bandegharaei, A.; Fu, J.; Mitropoulos, A. C.; Kyzas, G. Z. Use of Nanoparticles for Dye Adsorption: Review. *J. Dispersion Sci. Technol.* **2018**, *39*, 836−847.
(6) Baslak, C.; Arslan, G.; Kus, M.; Cengeloglu, Y. Removal of Rhodamine B from Water by Using CdTeSe Quantum Dot-Cellulose Membrane Composites. *RSC Adv.* **2016**, *6*, 18549−18557.
(7) Dong, W.; Lee, C. W.; Lu, X.; Sun, Y.; Hua, W.; Zhuang, G.; Zhang, S.; Chen, J.; Hou, H.; Zhao, D. Synchronous Role of Coupled Adsorption and Photocatalytic Oxidation on Ordered Mesoporous Anatase TiO_2-SiO_2 Nanocomposites Generating Excellent Degradation Activity of RhB Dye. *Appl. Catal., B* **2010**, *95*, 197−207.
(8) Khan, T. A.; Sharma, S.; Ali, I. Adsorption of Rhodamine B Dye from Aqueous Solution onto Acid Activated Mango (Magnifera Indica) Leaf Powder: Equilibrium, Kinetic and Thermodynamic Studies. *J. Toxicol. Environ. Health Sci.* **2011**, *3*, 286−297.
(9) Nagaraja, R.; Kottam, N.; Girija, C. R.; Nagabhushana, B. M. Photocatalytic Degradation of Rhodamine B Dye under UV/Solar Light Using ZnO Nanopowder Synthesized by Solution Combustion Route. *Powder Technol.* **2012**, *215*−*216*, 91−97.
(10) Vadivel, S.; Vanitha, M.; Muthukrishnaraj, A.; Balasubramanian, N. Graphene Oxide-BiOBr Composite Material as Highly Efficient Photocatalyst for Degradation of Methylene Blue and Rhodamine-B Dyes. *J. Water Process Eng.* **2014**, *1*, 17−26.
(11) Zhou, W.; Sun, S.; Jiang, Y.; Zhang, M.; Lawan, I.; Fernando, G. F.; Wang, L.; Yuan, Z. Template in Situ Synthesis of Flower-like BiOBr/Microcrystalline Cellulose Composites with Highly Visible-Light Photocatalytic Activity. *Cellulose* **2019**, *26*, 9529−9541.
(12) John, A.; Ko, H. U.; Kim, D. G.; Kim, J.; Fe, C.; Superparamagnetic, O. S.; Chen, L.; Berry, R. M.; Tam, K. C. Preparation of Cellulose-ZnO Hybrid Films by a Wet Chemical Method and Their Characterization. *Cellulose* **2011**, *18*, 675−680.
(13) Valencia, L.; Nomena, E. M.; Mathew, A. P.; Velikov, K. P. Biobased Cellulose Nanofibril-Oil Composite Films for Active Edible Barriers. *ACS Appl. Mater. Interfaces* **2019**, *11*, 16040−16047.
(14) Mohamed, M. A.; Salleh, W. N. W.; Jaafar, J.; Mohd Hir, Z. A.; Rosmi, M. S.; Abd. Mutalib, M.; Ismail, A. F.; Tanemura, M. Regenerated Cellulose Membrane as Bio-Template for in-Situ Growth of Visible-Light Driven C-Modified Mesoporous Titania. *Carbohydr. Polym.* **2016**, *146*, 166−173.
(15) Li, Q.; Zhou, D.; Zhang, P.; Man, P.; Tian, Z.; Li, Y.; Ai, S. The BiOBr/Regenerated Cellulose Composite Film as a Green Catalyst for Light Degradation of Phenol. *Colloids Surf., A* **2016**, *501*, 132−137.
(16) Budnyak, T. M.; Vlasova, N. N.; Golovkova, L. P.; Slabon, A.; Tertykh, V. A. Bile Acids Adsorption by Chitoan-Fumed Silica Enterosorbent. *Colloids Interface Sci. Commun.* **2019**, *32*, 100194.
(17) Budnyak, T. M.; Slabon, A.; Sipponen, M. H. Lignin−Inorganic Interfaces: Chemistry and Applications from Adsorbents to Catalysts and Energy Storage Materials. *ChemSusChem* **2020**. DOI: 10.1002/cssc.202000216.
(18) Budnyak, T. M.; Piątek, J.; Pylypchuk, I. V.; Klimpel, M.; Sevastyanova, O.; Lindström, M. E.; Gun'ko, V. M.; Slabon, A. Membrane-Filtered Kraft Lignin−Silica Hybrids as Bio-Based Sorbents for Cobalt(II) Ion Recycling. *ACS Omega* **2020**, *5*, 10847−10856.
(19) Sultan, S.; Abdelhamid, H. N.; Zou, X.; Mathew, A. P. CelloMOF: Nanocellulose Enabled 3D Printing of Metal−Organic Frameworks. *Adv. Funct. Mater.* **2019**, *29*, 1−12.
(20) Valencia, L.; Rosas, W.; Aguilar-Sanchez, A.; Mathew, A. P.; Palmqvist, A. E. C. Bio-Based Micro-/Meso-/Macroporous Hybrid Foams with Ultrahigh Zeolite Loadings for Selective Capture of Carbon Dioxide. *ACS Appl. Mater. Interfaces* **2019**, *11*, 40424−40431.
(21) Valencia, L.; Kumar, S.; Nomena, E. M.; Salazar-Alvarez, G.; Mathew, A. P. In-Situ Growth of Metal Oxide Nanoparticles on Cellulose Nanofibrils for Dye Removal and Antimicrobial Applications. *ACS Appl. Nano Mater.* **2020**. 37172.
(22) Yi, F.; Ma, J.; Lin, C.; Wang, L.; Zhang, H.; Qian, Y.; Zhang, K. Insights into the Enhanced Adsorption/Photocatalysis Mechanism of a $Bi_4O_5Br_2$/g-C_3N_4 Nanosheet. *J. Alloys Compd.* **2020**, *821*, 153557.
(23) Mao, D.; Ding, S.; Meng, L.; Dai, Y.; Sun, C.; Yang, S.; He, H. One-Pot Microemulsion-Mediated Synthesis of Bi-Rich $Bi_4O_5Br_2$ with Controllable Morphologies and Excellent Visible-Light Photocatalytic Removal of Pollutants. *Appl. Catal., B* **2017**, *207*, 153−165.
(24) Ji, M.; Di, J.; Ge, Y.; Xia, J.; Li, H. 2D-2D Stacking of Graphene-like g-C_3N_4/Ultrathin $Bi_4O_5Br_2$ with Matched Energy Band Structure towards Antibiotic Removal. *Appl. Surf. Sci.* **2017**, *413*, 372−380.
(25) Waetzig, G. R.; Horrocks, G. A.; Jude, J. W.; Villalpando, G. V.; Zuin, L.; Banerjee, S. Ligand-Mediated Control of Dopant Oxidation

State and X-ray Excited Optical Luminescence in Eu-Doped LaOCl. *Inorg. Chem.* **2018**, *57*, 5842−5849.
(26) Xu, J.; Mao, Y. G.; Liu, T.; Peng, Y. Synthesis of a Novel One-Dimensional BiOBr-$Bi_4O_5Br_2$ Heterostructure with a High Quality Interface and Its Enhanced Visible-Light Photocatalytic Activity. *CrystEngComm* **2018**, *20*, 2292−2298.
(27) Corkett, A. J.; Chen, Z.; Bogdanovski, D.; Slabon, A.; Dronskowski, R. Band Gap Tuning in Bismuth Oxide Carbodiimide Bi_2O_2NCN. *Inorg. Chem.* **2019**, *58*, 6467−6473.
(28) Kato, D.; Hongo, K.; Maezono, R.; Higashi, M.; Kunioku, H.; Yabuuchi, M.; Suzuki, H.; Okajima, H.; Zhong, C.; Nakano, K.; Abe, R.; Kageyama, H. Valence Band Engineering of Layered Bismuth Oxyhalides toward Stable Visible-Light Water Splitting: Madelung Site Potential Analysis. *J. Am. Chem. Soc.* **2017**, *139*, 18725−18731.
(29) Kageyama, H.; Hayashi, K.; Maeda, K.; Attfield, J. P.; Hiroi, Z.; Rondinelli, J. M.; Poeppelmeier, K. R. Expanding Frontiers in Materials Chemistry and Physics with Multiple Anions. *Nat. Commun.* **2018**, *9*. DOI: 10.1038/s41467-018-02838-4.
(30) Liu, D.; Yao, W.; Wang, J.; Liu, Y.; Zhang, M.; Zhu, Y. Enhanced Visible Light Photocatalytic Performance of a Novel Heterostructured $Bi_4O_5Br_2/Bi_{24}O_{31}Br_{10}/Bi_2SiO_5$ Photocatalyst. *Appl. Catal., B* **2015**, *172*−*173*, 100−107.
(31) Alansi, A. M.; Al-Qunaibit, M.; Alade, I. O.; Qahtan, T. F.; Saleh, T. A. Visible-Light Responsive BiOBr Nanoparticles Loaded on Reduced Graphene Oxide for Photocatalytic Degradation of Dye. *J. Mol. Liq.* **2018**, *253*, 297−304.
(32) Ao, Y.; Wang, K.; Wang, P.; Wang, C.; Hou, J. Synthesis of Novel 2D-2D p-n Heterojunction BiOBr/$La_2Ti_2O_7$ Composite Photocatalyst with Enhanced Photocatalytic Performance under Both UV and Visible Light Irradiation. *Appl. Catal., B* **2016**, *194*, 157−168.
(33) Huo, Y.; Zhang, J.; Miao, M.; Jin, Y. Solvothermal Synthesis of Flower-like BiOBr Microspheres with Highly Visible-Light Photocatalytic Performances. *Appl. Catal., B* **2012**, *111*−*112*, 334−341.
(34) Ahmad, A. Synthesis and Evaluation of Photocatalytic Properties of BiOBr for Wastewater Treatment Applications. Thesis, Department of Chemical and Biological EngineeringFaculty of Engineering University of Ottawa, 2013. DOI: 10.20381/ruor-3435.
(35) Davi, M.; Schrader, F.; Scholz, T.; Ma, Z.; Rokicinska, A.; Dronskowski, R.; Kustrowski, P.; Slabon, A. $SrTaO_2N$ Nanowire Photoanode Modified with a Ferrihydrite Hole-Storage Layer for Photoelectrochemical Water Oxidation. *ACS Appl. Nano Mater.* **2018**, *1*, 869−876.
(36) Ma, Z.; Thersleff, T.; Görne, A. L.; Cordes, N.; Liu, Y.; Jakobi, S.; Rokicinska, A.; Schichtl, Z. G.; Coridan, R. H.; Kustrowski, P.; Schnick, W.; Dronskowski, R.; Slabon, A. Quaternary Core-Shell Oxynitride Nanowire Photoanode Containing a Hole-Extraction Gradient for Photoelectrochemical Water Oxidation. *ACS Appl. Mater. Interfaces* **2019**, *11*, 19077−19086.
(37) Deng, J.; Su, Y.; Liu, D.; Yang, P.; Liu, B.; Liu, C. Nanowire Photoelectrochemistry. *Chem. Rev.* **2019**, *119*, 9221−9259.
(38) Ma, Z.; Konze, P.; KüPers, M.; Wiemer, K.; Hoffzimmer, D.; Neumann, S.; Kunz, S.; Simon, U.; Dronskowski, R.; Slabon, A. Elucidation of the Active Sites for Monodisperse FePt and Pt Nanocrystal Catalysts for P-WSe_2 Photocathodes. *J. Phys. Chem. C* **2020**, *124*, 11877−11885.
(39) Lu, C.; Jothi, P. R.; Thersleff, T.; Budnyak, T. M.; Rokicinska, A.; Yubuta, K.; Dronskowski, R.; Kuśtrowski, P.; Fokwa, B. P. T.; Slabon, A. Nanostructured Core-Shell Metal Borides-Oxides as Highly Efficient Electrocatalysts for Photoelectrochemical Water Oxidation. *Nanoscale* **2020**, *12*, 3121−3128.
(40) Lu, C.; Ma, Z.; Jäger, J.; Budnyak, T. M.; Dronskowski, R.; Rokicinska, A.; Kuśtrowski, P.; Pammer, F.; Slabon, A. NiO/Poly(4-Alkylthiazole)s Hybrid Interface for Promoting Spatial Charge Separation in Photoelectrochemical Water Reduction. *ACS Appl. Mater. Interfaces* **2020**, *26*, 29173−29180.
(41) Li, P.; Cao, W.; Zhu, Y.; Teng, Q.; Peng, L.; Jiang, C.; Feng, C.; Wang, Y. NaOH-Induced Formation of 3D Flower-Sphere BiOBr/$Bi_4O_5Br_2$ with Proper-Oxygen Vacancies via in-Situ Self-Template Phase Transformation Method for Antibiotic Photodegradation. *Sci. Total Environ.* **2020**, *715*, 136809.
(42) Di, J.; Ji, M.; Xia, J.; Li, X.; Fan, W.; Zhang, Q.; Li, H. $Bi_4O_5Br_2$ Ultrasmall Nanosheets in Situ Strong Coupling to MWCNT and Improved Photocatalytic Activity for Tetracycline Hydrochloride Degradation. *J. Mol. Catal. A: Chem.* **2016**, *424*, 331−341.
(43) Su, X.; Wu, D. Facile Construction of the Phase Junction of BiOBr and $Bi_4O_5Br_2$ Nanoplates for Ciprofloxacin Photodegradation. *Mater. Sci. Semicond. Process.* **2018**, *80*, 123−130.
(44) Ding, S.; Mao, D.; Yang, S.; Wang, F.; Meng, L.; Han, M.; He, H.; Sun, C.; Xu, B. Graphene-Analogue h-BN Coupled Bi-Rich $Bi_4O_5Br_2$ Layered Microspheres for Enhanced Visible-Light Photocatalytic Activity and Mechanism Insight. *Appl. Catal., B* **2017**, *210*, 386−399.
(45) Khan, S. B.; Alamry, K. A.; Marwani, H. M.; Asiri, A. M.; Rahman, M. M. Synthesis and Environmental Applications of Cellulose/ZrO_2 Nanohybrid as a Selective Adsorbent for Nickel Ion. *Composites, Part B* **2013**, *50*, 253−258.
(46) Awual, M. R.; Hasan, M. M.; Iqbal, J.; Islam, M. A.; Islam, A.; Khandaker, S.; Asiri, A. M.; Rahman, M. M. Ligand Based Sustainable Composite Material for Sensitive Nickel(II) Capturing in Aqueous Media. *J. Environ. Chem. Eng.* **2020**, *8*, 103591.
(47) Ahmed, J.; Rahman, M. M.; Siddiquey, I. A.; Asiri, A. M.; Hasnat, M. A. Efficient Hydroquinone Sensor Based on Zinc, Strontium and Nickel Based Ternary Metal Oxide (TMO) Composites by Differential Pulse Voltammetry. *Sens. Actuators, B* **2018**, *256*, 383−392.
(48) Hussain, M. M.; Rahman, M. M.; Asiri, A. M. Ultrasensitive and Selective 4-Aminophenol Chemical Sensor Development Based on Nickel Oxide Nanoparticles Decorated Carbon Nanotube Nanocomposites for Green Environment. *J. Environ. Sci. (Beijing, China)* **2017**, *53*, 27−38.
(49) Abdel-Latif, I. A.; Rahman, M. M.; Khan, S. B. Neodymium Cobalt Oxide as a Chemical Sensor. *Results Phys.* **2018**, *8*, 578−583.
(50) Rahman, M. M.; Khan, S. B.; Marwani, H. M.; Asiri, A. M. Selective Divalent Cobalt Ions Detection Using Ag_2O_3-ZnO Nanocones by ICP-OES Method for Environmental Remediation. *PLoS One* **2014**, *9*, 1−23.
(51) Jamal, A.; Rahman, M. M.; Khan, S. B.; Faisal, M.; Akhtar, K.; Rub, M. A.; Asiri, A. M.; Al-Youbi, A. O. Cobalt Doped Antimony Oxide Nano-Particles Based Chemical Sensor and Photo-Catalyst for Environmental Pollutants. *Appl. Surf. Sci.* **2012**, *261*, 52−58.
(52) Ahmed, J.; Rahman, M. M.; Siddiquey, I. A.; Asiri, A. M.; Hasnat, M. A. Selective Detection of Divalent Nickel Ions Based on Wet-Chemically Prepared Cs-Doped ZnO Nanosheets. *Superlattices Microstruct.* **2014**, *71*, 93−104.
(53) Awual, M. R.; Alharthi, N. H.; Hasan, M. M.; Karim, M. R.; Islam, A.; Znad, H.; Hossain, M. A.; Halim, M. E.; Rahman, M. M.; Khaleque, M. A. Inorganic-Organic Based Novel Nano-Conjugate Material for Effective Cobalt(II) Ions Capturing from Wastewater. *Chem. Eng. J.* **2017**, *324*, 130−139.
(54) Katowah, D. F.; Rahman, M. M.; Hussein, M. A.; Sobahi, T. R.; Gabal, M. A.; Alam, M. M.; Asiri, A. M. Ternary Nanocomposite Based Poly(Pyrrole-Co-O-Toluidine), Cobalt Ferrite and Decorated Chitosan as a Selective Co^{2+} Cationic Sensor. *Composites, Part B* **2019**, *175*, 107175.
(55) Karim, Z.; Svedberg, A.; Lee, K. Y.; Khan, M. J. Processing-Structure-Property Correlation Understanding of Microfibrillated Cellulose Based Dimensional Structures for Ferric Ions Removal. *Sci. Rep.* **2019**, *9*, 1−12.
(56) Cristiano, E.; Hu, Y. J.; Siegfried, M.; Kaplan, D.; Nitsche, H. A Comparison of Point of Zero Charge Measurement Methodology. *Clays Clay Miner.* **2011**, *59*, 107−115.
(57) Samad, J. E.; Hashim, S.; Ma, S.; Regalbuto, J. R. Determining Surface Composition of Mixed Oxides with PH. *J. Colloid Interface Sci.* **2014**, *436*, 204−210.
(58) Pashai Gatabi, M.; Milani Moghaddam, H.; Ghorbani, M. Point of Zero Charge of Maghemite Decorated Multiwalled Carbon

Nanotubes Fabricated by Chemical Precipitation Method. *J. Mol. Liq.* **2016**, *216*, 117−125.
(59) Patel, E.; Lynch, C.; Ruff, V.; Reynolds, M. Co-Exposure to Nickel and Cobalt Chloride Enhances Cytotoxicity and Oxidative Stress in Human Lung Epithelial Cells. *Toxicol. Appl. Pharmacol.* **2012**, *258* (3), 367−375.
(60) Marchenko, Z. *Photometric Determination of Elements*; Mir: Moscow, 1971 (in Russian).
(61) Derylo-Marczewska, A.; Miroslaw, K.; Marczewski, A. W.; Sternik, D. Studies of Adsorption Equilibria and Kinetics of O-, m-, p-Nitro- and Chlorophenols on Microporous Carbons from Aqueous Solutions. *Adsorption* **2010**, *16*, 359−375.
(62) Marczewski, A. W. Application of Mixed Order Rate Equations to Adsorption of Methylene Blue on Mesoporous Carbons. *Appl. Surf. Sci.* **2010**, *256*, 5145−5152.
(63) Lagrergen, S. Zur Theorie Der sogenannten Adsorption gelöster Stoffe, Kungliga Svenska Vetenskapsakademiens. *Handlingar* **1898**, *24*, 1−39.
(64) Keller, E.; Ketterer, J.; Krämer, V. Crystal Structure and Twinning of $Bi_4O_5Br_2$. *Z. Kristallogr. - Cryst. Mater.* **2001**, *216*, 595−599.
(65) Sillen, L.. Svensk Kemisk Tidskrift. 1941, *53*, 39−43.
(66) Zheng, C.; He, G.; Xiao, X.; Lu, M.; Zhong, H.; Zuo, X.; Nan, J. Selective Photocatalytic Oxidation of Benzyl Alcohol into Benzaldehyde with High Selectivity and Conversion Ratio over $Bi_4O_5Br_2$ Nanoflakes under Blue LED Irradiation. *Appl. Catal., B* **2017**, *205*, 201−210.
(67) Bennettand, H.; Ouver, G. J. High Resolution XPS of Organic Polymers: The Scienta ESCA300 Database (Beamson, G.; Briggs, D.). *J. Chem. Educ.* **1993**, *70*, A25.
(68) Li, R.; Xie, F.; Liu, J.; Wang, Y.; Wang, Y.; Zhang, X.; Fan, C. Synthesis of $Bi_4O_5Br_2$ from Reorganization of BiOBr and Its Excellent Visible Light Photocatalytic Activity. *Dalt. Trans.* **2016**, *45*, 9182−9186.
(69) Di, J.; Xia, J.; Ji, M.; Yin, S.; Li, H.; Xu, H.; Zhang, Q.; Li, H. Controllable Synthesis of $Bi_4O_5Br_2$ Ultrathin Nanosheets for Photocatalytic Removal of Ciprofloxacin and Mechanism Insight. *J. Mater. Chem. A* **2015**, *3*, 15108−15118.
(70) Zalecki, R.; Woch, W. M.; Kowalik, M.; Kołodziejczyk, A. Bismuth Valence in a $Tl_{0.7}Bi_{0.3}Sr_{1.6}Ba_{0.4}CaCu_2O_y$ Superconductor from X-Ray Photoemission Spectroscopy. *Acta Phys. Pol., A* **2010**, *118*, 393−395.
(71) Cai, L.; Zhang, G.; Zhang, Y.; Wei, Y. Mediation of Band Structure for $BiOBr_xI_{1-x}$ Hierarchical Microspheres of Multiple Defects with Enhanced Visible-Light Photocatalytic Activity. *CrystEngComm* **2018**, *20*, 3647−3656.
(72) Li, S.; Ye, G.; Chen, G. Low-Temperature Preparation and Characterization of Nanocrystalline Anatase TiO_2. *J. Phys. Chem. C* **2009**, *113*, 4031−4037.
(73) Mohamed, M. A.; Salleh, W. N. W.; Jaafar, J.; Ismail, A. F.; Abd. Mutalib, M.; Jamil, S. M. Feasibility of Recycled Newspaper as Cellulose Source for Regenerated Cellulose Membrane Fabrication. *J. Appl. Polym. Sci.* **2015**, *132*, 1−10.
(74) Li, S.; Ye, G.; Chen, G.; Mohamed, M. A.; Salleh, W. N. W.; Jaafar, J.; Ismail, A. F.; Abd. Mutalib, M.; Jamil, S. M. Feasibility of Recycled Newspaper as Cellulose Source for Regenerated Cellulose Membrane Fabrication. *J. Appl. Polym. Sci.* **2015**, *132*, 1−10.
(75) Du, M.; Du, Y.; Feng, Y.; Yang, K.; Lv, X.; Jiang, N.; Liu, Y. Facile Preparation of BiOBr/Cellulose Composites by in Situ Synthesis and Its Enhanced Photocatalytic Activity under Visible-Light. *Carbohydr. Polym.* **2018**, *195*, 393−400.
(76) Awang, N. A.; Wan Salleh, W. N.; Ismail, A. F.; Yusof, N.; Aziz, F.; Jaafar, J. Adsorption Behavior of Chromium(VI) onto Regenerated Cellulose Membrane. *Ind. Eng. Chem. Res.* **2019**, *58*, 720−728.
(77) Choi, H. Y.; Bae, J. H.; Hasegawa, Y.; An, S.; Kim, I. S.; Lee, H.; Kim, M. Thiol-Functionalized Cellulose Nanofiber Membranes for the Effective Adsorption of Heavy Metal Ions in Water. *Carbohydr. Polym.* **2020**, *234*, 115881.
(78) Qiao, L.; Li, S.; Li, Y.; Liu, Y.; Du, K. Fabrication of Superporous Cellulose Beads via Enhanced Inner Cross-Linked Linkages for High Efficient Adsorption of Heavy Metal Ions. *J. Cleaner Prod.* **2020**, *253*, 120017.
(79) Hajeeth, T.; Vijayalakshmi, K.; Gomathi, T.; Sudha, P. N.; Anbalagan, S. Adsorption of Copper(II) and Nickel(II) Ions from Aqueous Solution Using Graft Copolymer of Cellulose Extracted from the Sisal Fiber with Acrylic Acid Monomer. *Compos. Interfaces* **2014**, *21*, 75−86.
(80) Hassan, H. S.; Elkady, M. F.; Farghali, A. A.; Salem, A. M.; AbdEl-Hamid, A. I. Fabrication of Novel Magnetic Zinc Oxide Cellulose Acetate Hybrid Nano-Fiber to Be Utilized for Phenol Decontamination. *J. Taiwan Inst. Chem. Eng.* **2017**, *78*, 307−316.
(81) Hamad, A. A.; Hassouna, M. S.; Shalaby, T. I.; Elkady, M. F.; Abd Elkawi, M. A.; Hamad, H. A. Electrospun Cellulose Acetate Nanofiber Incorporated with Hydroxyapatite for Removal of Heavy Metals. *Int. J. Biol. Macromol.* **2020**, *151*, 1299−1313.
(82) Piątek, J.; de Bruin-Dickason, C. N.; Jaworski, A.; Chen, J.; Budnyak, T.; Slabon, A. Glycine-Functionalized Silica as Sorbent for Cobalt(II) and Nickel(II) Recovery. *Appl. Surf. Sci.* **2020**, *530*, 147299.

https://dx.doi.org/10.1021/acsami.0c12739
ACS Appl. Mater. Interfaces 2020, 12, 42891−42901